

A Global Assessment of the Spatial Distribution of Precipitation Occurrence

MARK SMALLEY AND TRISTAN L'ECUYER

University of Wisconsin–Madison, Madison, Wisconsin

(Manuscript received 6 January 2015, in final form 24 August 2015)

ABSTRACT

The spatial distribution of precipitation occurrence has important implications for numerous applications ranging from defining cloud radiative effects to modeling hydrologic runoff, statistical downscaling, and stochastic weather generation. This paper introduces a new method of describing the spatial characteristics of rainfall and snowfall that takes advantage of the high sensitivity and high resolution of the W-band cloud precipitation radar aboard *CloudSat*. The resolution dependence of precipitation occurrence is described by a two-parameter exponential function defined by a shape factor that governs the variation in the distances between precipitation events and a scale length that represents the overall probability of precipitation and number density of distinct events.

Geographic variations in the shape factor and scale length are consistent with large-scale circulation patterns and correlate with environmental conditions on local scales. For example, a large contrast in scale lengths between land and ocean areas reflects the more extensive, widespread nature of precipitation over land than over ocean. An analysis of warm rain in the southeast Pacific reveals a shift from frequent isolated systems to less frequent but more regularly spaced systems along a transect connecting stratocumulus and trade cumulus cloud regimes. A similar analysis during the Amazon wet season reveals a relationship between the size and frequency of convection and zonal wind direction with precipitation exhibiting a more oceanic character during periods of westerly winds. These select examples demonstrate the utility of this approach for capturing the sensitivity of the spatial characteristics of precipitation to environmental influences on both local and larger scales.

1. Introduction

The spatial distribution of clouds and precipitation has long been recognized as having important implications for the earth–atmosphere system. Precipitation and the associated cloud masses affect both local energy budgets and large-scale circulations through reflection and absorption of radiation and the release and transport of latent heat. While global mean precipitation and its response to realistic climate forcing scenarios is being modeled increasingly well by the leading global circulation models (GCM), changes in precipitation frequency and volume at regional scales remain a major source of uncertainty in climate predictions (Stephens et al. 2010; Flato et al. 2013).

Precipitation occurrence patterns also play an important role in accurately modeling runoff and infiltration at the catchment scale in numerical weather prediction

models. Hydrologists require finescale, detailed knowledge of the frequency, volume, and spatial distribution of precipitation to assess the local impacts of impending extreme weather events or to adapt to climate change (Fowler et al. 2007). Practical decision-making for infrastructure and land use under forecasts of increasing or decreasing precipitation volume can only be made with this localized information (Milly et al. 2008). It can be imagined that even if the monthly average volume or frequency of precipitation does not change in an area, changes in the spatial and temporal distribution may still be important for agriculture, flooding, and other hydrologic applications. Unfortunately, current computation speeds and a lack of explicit representation of microphysics require the use of either dynamical or statistical methods to downscale highly variable processes such as clouds and precipitation to fine scales in GCMs.

This problem may be partially addressed using new tools such as global cloud-resolving models (GCRM) and multimodel frameworks (MMF) that offer potential for more explicit representation of cloud and precipitation processes on global scales. However, these

Corresponding author address: Mark Smalley, 1225 W. Dayton St., Madison, WI 53706.
E-mail: smalley2@wisc.edu

tools are currently too computationally expensive to run for long periods at the high resolution needed to study individual catchments and also require observational validation. An alternative approach to creating subgrid precipitation spatial distributions is the implementation of stochastic weather generation models that prescribe precipitation fields for the given circulation conditions (Wilks 2010). Developing and evaluating such models is an active area of research (Fowler et al. 2007), motivating the need for observational benchmarks of the spatial character of precipitation globally and for knowledge of the local- and large-scale factors influencing the spatial distribution of precipitation.

The large range of relevant precipitation scales, from individual convective cells to synoptic-scale frontal systems, makes it desirable to determine an analytical relation that describes the variation of precipitation distributions across these scales. Many previous works have focused on the self-repeating or fractal nature of precipitation events (Tao and Barros 2010; Ferraris et al. 2003; O'Brien et al. 2013), while others have found that the variance of precipitation does not always follow a single pattern through all scales (Marani 2005). Gebremichael et al. (2008) used precipitation radar (PR) retrievals from the Tropical Rainfall Measuring Mission (TRMM) to describe the spatial distribution of rainfall in the tropics with scale-invariant relations. They found a land–ocean contrast in their distribution parameters: precipitation over tropical land tends to break from scale invariance more than precipitation over the tropical ocean.

While advantageous because of its 2D imaging and fully diurnal sampling, the Ku-band TRMM PR likely misses much of the light and isolated rainfall that dominates precipitation frequency in the radiatively important stratocumulus regions, which also makes up a significant fraction of the total rain frequency around the globe (Berg et al. 2010; Haynes et al. 2009). In addition, the TRMM PR only samples the region equatorward of about 35°, leaving a large fraction of the midlatitudes and polar regions devoid of radar-based estimates of precipitation occurrence. By virtue of its highly sensitive 94-GHz frequency, ~1.5-km instantaneous field of view (FoV), and 98° orbit inclination, the *CloudSat* Cloud Profiling Radar (CPR) can mitigate these deficiencies, though with significantly reduced sampling due to a lack of scanning capability. The CPR operated nominally for about 4.5 years and has continued to operate during the daytime for another 5 years, providing sufficient data volume to sample monthly and seasonal variations in the distribution of precipitation around the globe. This study will utilize observations from four complete annual cycles from 2007 to 2010, when the CPR was operating at full capacity during its day and night overpasses.

The specific datasets used will be described in detail in section 2. Section 3 introduces a new approach for describing the spatial distribution of precipitation using binary precipitation/no-precipitation discrimination from *CloudSat* observations, and section 4 explains the physical mechanisms that create variation in the spatial distribution parameters. The spatial distribution and day/night variability of the scale dependence of precipitation around the globe is documented in section 5. Sections 6 and 7 illustrate the variations of the precipitation scaling relationships of precipitation in the geographic transition between stratocumulus and trade cumulus cloud types in the southeast Pacific subtropics, while section 8 investigates the relationship between zonal wind speed and the spatial character of precipitation in the Amazon. Key results are summarized in section 9 to place the technique in the context of ongoing efforts to improve the representation of the spatial characteristics of precipitation in hydrological, weather, and climate models.

2. Data

The primary data used in this study are precipitation flags from the *CloudSat* 2C-PRECIP-COLUMN (2CPC) retrievals spanning the years from 2007 to 2010. The 2CPC dataset is available through the CloudSat Data Processing Center (<http://www.cloudsat.cira.colostate.edu>). With a sensitivity of about -30 dBZ, the 94-GHz CPR is very sensitive to cloud and precipitating hydrometeors (Tanelli et al. 2008). In this analysis, *CloudSat* pixels determined as “rain probable,” “rain certain,” “snow certain,” or “mixed certain” in the 2CPC Precip_flag are considered to be precipitating and the remaining successful retrievals are considered to be nonprecipitating, creating a binary precipitation/no-precipitation discriminator. The corresponding thresholds in near-surface attenuation-corrected reflectivity over open ocean for each of these precipitation categories are -7.5 , 0 , -5 , and -5 dBZ, respectively (Haynes et al. 2009). Retrievals over land are slightly more complicated because of uncertainties in the path-integrated attenuation of the CPR beam and the surface backscatter cross section, but similar thresholds are used in the lowest cloud layer above the fifth range bin above the surface. A detailed description of the overland retrieval can be found in Smalley et al. (2014). Rain probable FoVs are included primarily to enhance detection in marine stratocumulus areas where warm rain often falls in the form of drizzle. Some of this light precipitation flagged as rain probable may evaporate before reaching the surface; while not contributing to rain volume, the virga redistributes boundary layer temperature and water vapor and affects cloud albedo by depleting cloud water and aerosols. This analysis likely captures all

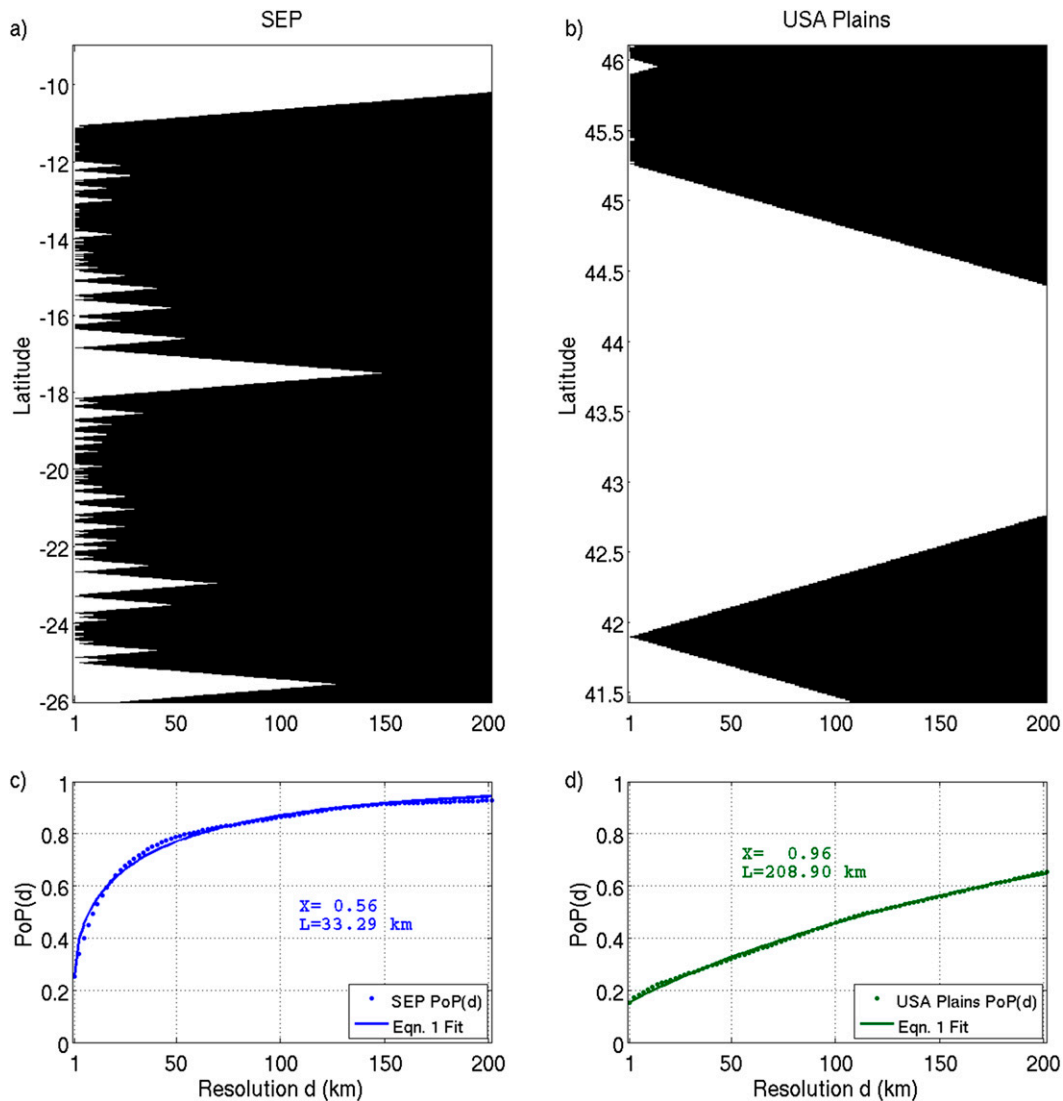


FIG. 1. The relationship between resolution and PoP for two *CloudSat* orbits that passed over the (a),(c) SEP stratocumulus decks (12 Dec 2007; orbit 05897) and (b),(d) U.S. plains stratiform precipitation regimes (2 Dec 2007; orbit 08489). In (a) and (b), black shading represents precipitation at each resolution along the x axis. The native *CloudSat* resolution is seen at about $d = 1.1$ km in all plots.

examples from segments of *CloudSat* observations over the southeast Pacific (SEP) and central U.S. plains are presented in Fig. 1 for comparison. These regions are chosen because they exhibit very different precipitation regimes in their respective winter seasons and are generally representative of the extreme ends of the global spectrum of precipitation characteristics. Precipitation occurrence vectors are presented for resolutions ranging from the native *CloudSat* resolution to 201 km in length. As is observed when comparing Table 2 to Table 1, the higher CPE density in the SEP (78 versus 5 events) causes the PoP to rise more quickly than in the case of the U.S. plains. The increased PoP(1) ($\sim 25\%$ vs $\sim 15\%$) in the

SEP adds to this effect. As the resolution degrades at longer d , the slope of PoP(d) decreases in both regions. The difference in the slopes at high and low resolution is related to the relative CPE spacing in the considered data, as initially distinct CPEs become indistinguishable at coarse resolutions. These are the primary factors governing the shape of observed relationships between PoP and d .

It is unlikely that a single overpass will represent either the characteristic relative event spacing or number of events. Analyses subsequent to those in Fig. 1 include data from many overpasses to better represent the statistical relationships instead of being controlled by the high variance of near-instantaneous weather.

The utility of this process becomes evident when the PoP is plotted as a function of d as shown in Figs. 1c and 1d. The relationship is well approximated by the exponential function

$$\text{PoP}(d) = 1 - P_{\text{co}} \exp \left[- \left(\frac{d-1}{L} \right)^X \right]. \quad (1)$$

Here, d is the search length (proxy for resolution) and P_{co} is the native-resolution fraction of nonprecipitating *CloudSat* pixels, $P_{\text{co}} = 1 - \text{PoP}(1)$. Equation (1) describes how the probability of precipitation varies with spatial resolution. In this framework the spatial characteristics of precipitation occurrence are described by just two parameters: a shape factor X and a scale length L . The shape factor is unitless and the scale length is multiplied by a factor of 1.1 to convert the units from number of FoVs to a physical search length in kilometers.

Figures 1c and 1d present the exponential fit, shape factor, and scale length for the segments shown in Figs. 1a and 1b. These examples show that even individual overpasses with widely different spatial distributions can be described accurately by Eq. (1). It should be noted, however, that the goal of this study is to capture variations in the statistical properties of precipitation spatial distributions across different regions. This requires a collection of enough individual overpasses in each region to obtain an accurate representation of precipitation prevalence, characteristic spacing, and the number density of events. In particular, the U.S. plains (and other land areas) will be shown to exhibit scale lengths much longer than displayed in Fig. 1b. The amount of data necessary to resolve such long scale lengths is greater than the number of FoVs in each individual *CloudSat* segment, so more overpasses are required to properly capture the relationship between PoP and d and to derive the appropriate shape factor and scale length. The shape factor is related to characteristic event spacing, so many events (and therefore their separations) must be obtained before the shape factor may be reliably estimated. Through statistical tests (not shown), it was demonstrated that about 75 000 to 120 000 FoVs are necessary to obtain convergence in the distribution parameters depending on season, location, and characteristic weather regime. The relationships between the resulting distribution parameters and a more complete spectrum of environmental factors are the focus of an ongoing study.

One immediate application of this methodology is that the resulting parameterization, $\text{PoP}(d)$, describes the probability of observing precipitation along any 1D grid box at any prescribed resolution. This has utility in understanding the effects of model resolution on fractional precipitation in weather and climate models. Stephens

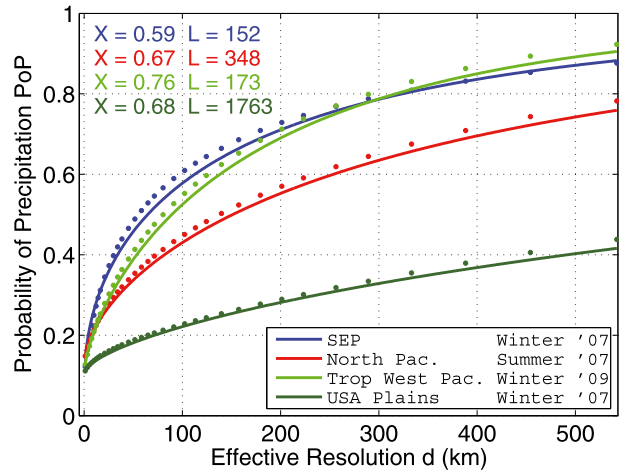


FIG. 2. Effects of resolution on the probability of precipitation and distribution parameters from Eq. (1) for four regions: North Pacific (30°–60°N, 160°–220°E), tropical west Pacific (10°S–10°N, 130°–190°E), U.S. plains (35°–50°N, 260°–275°E), and southeast Pacific (25°–10°S, 250°–284°E).

et al. (2010) showed that using the correct averaging scale is important when comparing precipitation areal coverage in GCMs. They further recognized that the averaging scale required to relate the probability of precipitation between models with different spatial resolutions depends on the spatial distribution of precipitation in that area, something that may change with season, location, and weather regime. A further application of the methodology outlined above is, therefore, to relate the two fit parameters to the large-scale and local thermodynamic environment so that they may be used to downscale precipitation occurrence to resolutions finer than model grid boxes. The distribution parameters represent a new method of characterizing spatial distributions of event occurrence, offering insights into factors controlling the relative spacing and number density of precipitation events. This second application will be explored in greater detail below.

4. Physical interpretation of distribution parameters

Similar approaches to establishing the spatial characteristics of clouds and rainfall in more limited regions have been developed by others (e.g., Marchand 2012; Kundu and Siddani 2011; Schleiss et al. 2011). However, the method of resolution degradation employed here leads to subtle differences in the interpretation of the resulting shape factor and scale length that warrant additional discussion prior to examining their spatial and temporal distributions.

Figure 2 illustrates how the regression outlined in Eq. (1) responds to precipitation distributions from different

weather regimes that have similar PoP at the native *CloudSat* resolution. The rate of increase in PoP with increasing d varies substantially with region but the exponential fit captures this variation very well (R^2 values are above 0.997 for all four of these cases). The results can be interpreted as follows. As d increases from the native *CloudSat* resolution, PoP increases as illustrated in Tables 1 and 2 and in Figs. 1a and 1b. In regions with broken precipitation (e.g., SEP), there are more distinct CPEs that increase the rate at which precipitation occurrence increases with increasing d (e.g., Table 2). Accordingly, PoP initially increases rapidly but slows when the resolution is degraded enough that initially distinct CPEs become indistinguishable. The initial rate of increase is much weaker in regions populated by large-scale stratiform systems for which there are relatively fewer CPEs (e.g., Table 1). This is the case with large-scale systems typical of those observed over the U.S. plains in the winter months. The scale length L describes the resolution at which the PoP increases to within a factor of $1/e$ of unity from the high-resolution PoP(1). The shape factor X represents the deviation of the curve from a standard exponential ($X = 1$). For precipitation, the shape factor generally takes values less than one, so PoP increases more rapidly than would be represented by a standard exponential at resolutions higher than L and less rapidly at coarser resolutions.

To more precisely illustrate the specific factors controlling the shape factor and scale length, synthetic binary rain datasets were generated as an autocorrelated vector. High-resolution synthetic rain flags were created to obey the following rules: if the rain flag for a given synthetic pixel has a value of 0 (nonraining), the probability of the next pixel also being 0 is very high: 0.998 to reflect the high autocorrelation of nonrainy pixels. On the other hand, if the current pixel is 1 (raining), the probability of the next pixel being rainy is slightly lower but still very high: 0.911. If the synthetic dataset is long enough, the resulting fraction of simulated scenes with a value of 1 is about 10%. Many combinations of these autocorrelations can produce PoP(1) = 10%, but these values were chosen because they result in shape factors and scale lengths that are similar to what are observed in the *CloudSat* data. Autocorrelation values can be adjusted to obtain different high-resolution PoP values [e.g., 0.990 and 0.960 for PoP(1) = 20%] so, with a long enough synthetic dataset, the choice of the two autocorrelations defines the resulting PoP(1). Choosing the two autocorrelations to be identical will result in, on average, a synthetic dataset with PoP(1) = 50%. The sequence is initialized by a nonraining pixel, and a sizable segment of the beginning of the synthetic data is removed to eliminate the effects of creating the first

pixel without information from a previous synthetic pixel. The remaining pixels are broken into smaller segments from which distribution parameters can be computed via Eq. (1). The result is a realistic rain field that follows a similar spatial distribution to naturally occurring precipitation. This is analogous to the “weather generator” procedure one would use to create a realistic precipitation series that obeys the characteristics predicted by the exponential distribution with the corresponding shape factor and scale length, an application that will be investigated in future work.

Figure 3 illustrates how the shape factor and scale length are affected by characteristics of the spatial distribution of precipitation. Figure 3a shows that the shape factor is most strongly influenced by changes in the distribution of distances between precipitation events, represented here by the coefficient of variation (CoV; defined as the standard deviation divided by the mean). High values of CoV result in low shape factors. This is consistent with the fact that if the CoV is low, many distances between CPEs are similar and CPEs appear indistinguishable at comparable resolutions, causing a sharper transition toward decreased slopes in Eq. (1).

The interpretation of the scale length is slightly more complicated. Figure 3b shows that the scale length exhibits a clear trend toward lower values as the number density of CPEs increases. For a fixed PoP(1), the presence of fewer but larger CPEs requires coarser resolutions to be simulated before the PoP approaches unity resulting in longer scale lengths. A lower value of PoP(1) will also lead to longer scale lengths. As expected, the CPE density is highly correlated with PoP(1) so these two effects combine to yield a much larger range in L than X in observed precipitation.

Figures 3c and 3d show that the relationships identified in the simulated precipitation distributions are also apparent in observations. Here, precipitation detections from the regions and time periods shown in Fig. 2 are broken into segments (each still containing many individual overpasses), fitted, and plotted against their respective controlling factors. The linear regression lines are included for guidance and do not represent an absolute slope or intercept. The U.S. plains region is recognizable by its very long scale lengths in the winter months of 2007, indicating a low precipitation occurrence and/or a low density of CPEs. Smalley et al. (2014) found that *CloudSat* observes high rates of precipitation over the United States when the near-surface air temperature is below zero, indicating that this signal is likely due to the stratiform frontal nature of winter precipitation in this region. Conversely, much shorter scale lengths characterize the frequent isolated precipitation in the SEP. Precipitation in this region also

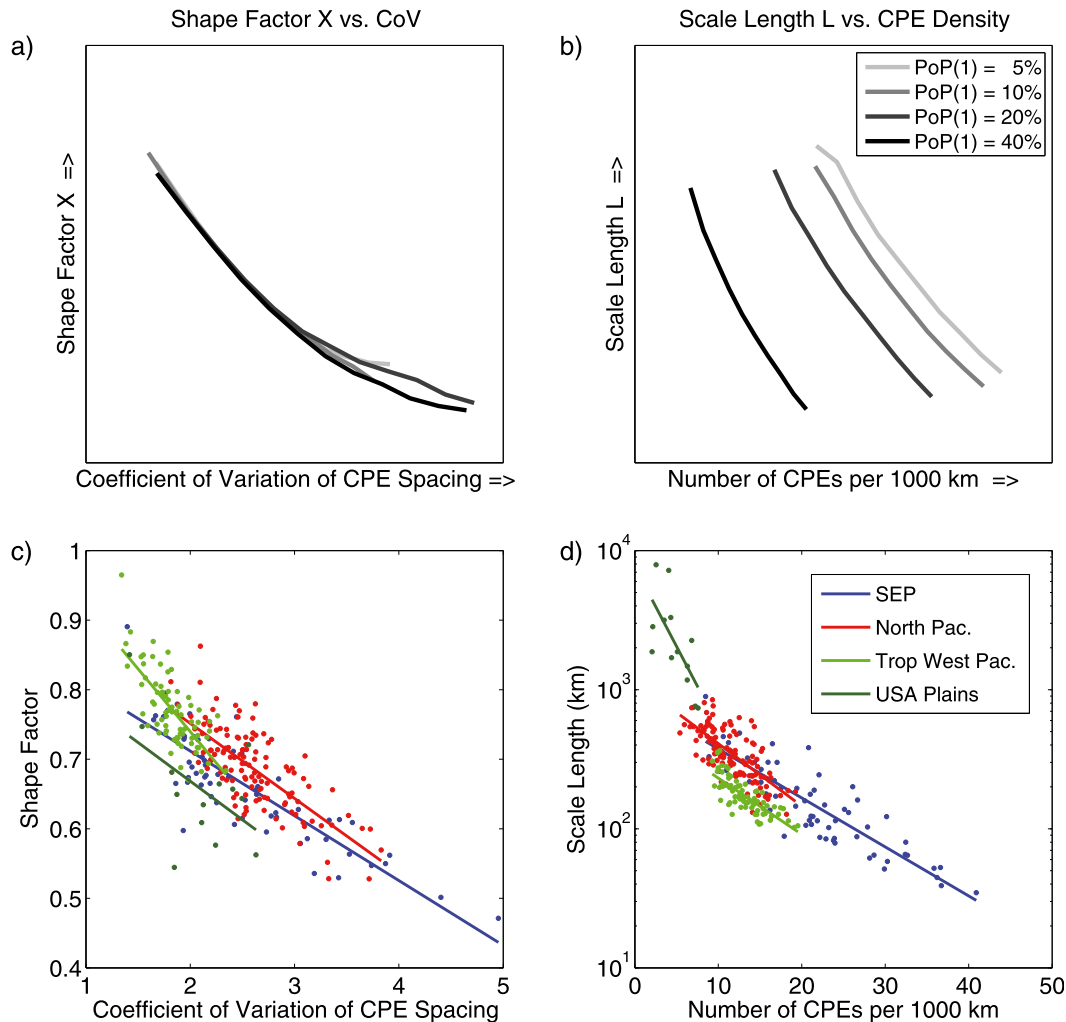


FIG. 3. Physical interpretation of the shape factor X and scale length L in terms of properties of the spatial distribution of precipitation. (a),(b) Data were computed using synthetic data described in the text. (c),(d) Scatterplots of distribution properties and spatial parameters for the regions and time periods shown in Fig. 2. Each pair of distribution parameters are computed from a separate set of 10 000 resolution-degraded FoVs: synthetic FoVs in (a) and (b) and observed FoVs in (c) and (d).

exhibits a much wider range of shape factors, highlighting the more variable degree of precipitation organization, owing to factors that will be discussed in greater detail below.

To summarize, this method of degrading the resolution of binary precipitation discrimination preserves finescale spatial characteristics of precipitation. The form of the resulting PoP versus resolution can be reliably modeled by an exponential function with two free parameters, a shape factor X and scale length L . The shape factor represents the PDF of distances between distinct precipitation events, and the scale length represents the number density of those events and the high-resolution probability of precipitation. A broken precipitation field with high variance in event spacing leads

to a small shape factor and vice versa. The scale length is determined by the overall rate of increase toward 100% PoP as d increases. If PoP(1) is low and there are few CPEs, the resulting scale length is long because there are relatively few CPE edges to which additional precipitation may be added via resolution degradation, and it therefore takes long search lengths (coarse resolutions) for the PoP to approach unity.

There are some important caveats associated with this analysis. First, the resolution degradation method utilized in this study focuses on characterizing the spatial distribution of precipitation occurrence within the region of interest as opposed to the distribution of precipitation intensity. In principle, the scale dependence of precipitation intensity could be examined by averaging

CloudSat reflectivities before running the *CloudSat* precipitation algorithm, but such an approach places a disproportionate amount of influence on FoVs containing heavy precipitation. While this may be of interest for several applications (e.g., effects of sensor resolution on retrieved precipitation rates), it does not represent the spatial characteristics of precipitation occurrence within a grid box that are particularly important for modeling radiative effects of precipitation efficiency, stochastic weather generation, and hydrologic modeling that are the targets of this study. In addition, strong attenuation at W band limits the upper range of precipitation intensities that can be accurately retrieved from *CloudSat* observations, requiring the use of more complicated multi-instrument merging techniques like those presented in Berg et al. (2010) to accurately represent the full rain-rate PDF. Ultimately, a combination of occurrence and intensity-centric methods are likely required to fully address the problem of precipitation downscaling on global scales, but this paper focuses on the former as it has received less attention in the literature to date.

A comment is also warranted concerning constraints imposed by trade-offs between resolution and sampling. Figure 2 illustrates the effects of simulating resolutions of more than 500 km or about 5° in latitude, a range that can experience considerable changes in the characteristics of precipitation, both instantaneously and climatologically. To obtain a more localized picture of the spatial characteristics, it is advantageous to limit the influence that a particular region can have on neighboring regions. The distribution parameters are found to be generally insensitive to increasing the maximum search length beyond 200 km. Therefore, to better represent local precipitation processes, the maximum resolution is set to 201 km for the remainder of the analysis. Finally, regions with very low numbers of CPEs and/or PoP(1) reduce the signal-to-noise ratio of the analysis. To remedy this, subsequent analyses ignore geographic areas with less than 1% PoP(1), as determined by *CloudSat*.

5. Global, seasonal, and diurnal variability

Figure 4 shows global maps of the seasonal variation of PoP(1), the shape factor, and the scale length for 2007–10. This figure was created by compiling precipitation statistics for all 2° areas sampled by *CloudSat* between 80°S and 80°N. Resolution-degraded precipitation flags belonging to each area are used to compute PoP versus d relationships, which are then used to compute the distribution parameters shown in the second and third columns. To better highlight large-scale

patterns, high spatial variability in each plot has been removed by applying the filter defined in Eq. (2):

$$W = \begin{pmatrix} 0 & 1 & 1 & 1 & 0 \\ 1 & 5 & 5 & 5 & 1 \\ 1 & 5 & 7 & 5 & 1 \\ 1 & 5 & 5 & 5 & 1 \\ 0 & 1 & 1 & 1 & 0 \end{pmatrix}. \quad (2)$$

Casual inspection of the second column (shape factor) and third column (scale length) suggests that the structure parameters are able to discern broad characteristics of large-scale circulation regimes and their annual cycles around the globe. For instance, the isolated but frequent convective nature of precipitation in the ITCZ favors short scale lengths, on the order of 100 km, and smaller shape factors than the surrounding oceans. Longer scale lengths south of the ITCZ indicate decreasing PoP(1), which is characteristic of large-scale descent.

The midlatitude oceanic storm tracks are manifested through reduced values of shape factor and scale length. Perturbations in the polar front that create southern midlatitude cyclones are large-scale disturbances that produce widespread precipitation systems. Many of these long-lived southern storm-track precipitation systems are spun up by vortex stretching on the lee side of the southern Andes Mountains at around 45°S (Hoskins and Hodges 2005). However, the observed PoP(1) is low in the regions near the coast of Argentina, so scale lengths remain long in the downstream area. Since precipitation is common in the rest of the storm-track regions in all seasons, the relationship between scale length and PoP(1) translates to short scale lengths, as especially evident in the austral winter months of June–August (JJA).

Characteristic precipitation patterns are also evident in the SEP and southeast Atlantic stratocumulus regions. Low values of the shape factor in these regions are indicative of precipitation distributions consisting of high variance in CPE spacing. The effect is most pronounced during the local winter and spring, coinciding with maxima in PoP(1), CPE density, and CoV (investigated below for SEP). These regions are dominated by large-scale subsidence and experience a stable middle troposphere, which caps convection at the boundary layer with a strong temperature inversion that enables a persistent stratocumulus cloud deck (Wood 2012). Cloud-top radiative cooling results in downward convection and a maintained upward transport of water vapor through the well-mixed surface-coupled boundary layer, forming frequent warm rain that falls as drizzle. The precipitation in the stratocumulus areas is often

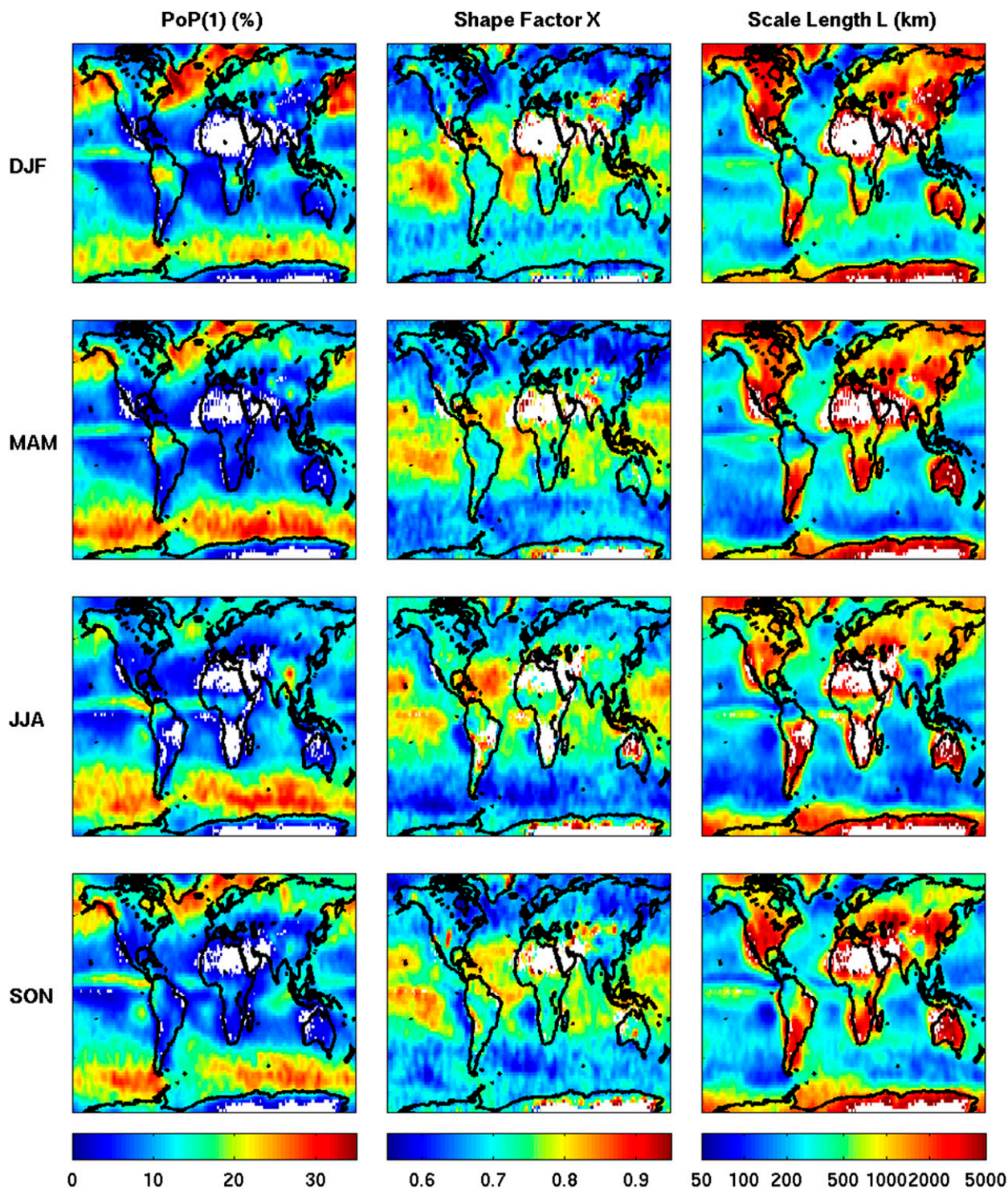


FIG. 4. Seasonal maps of PoP(1), shape factor, and scale length on a $2^\circ \times 2^\circ$ geographic grid for all *CloudSat* orbits from 2007 to 2010. The plotted values have been filtered as defined in Eq. (2) to emphasize large-scale variations.

very light and originates from low heights in the marine boundary layer. The signal from these areas is largely absent from the analysis if the rain probable detections are omitted (not shown) owing to the importance of drizzle to the overall precipitation spatial distributions in these areas.

In these environments, pockets of open cells (POCs) can significantly contribute to precipitation occurrence and volume, where convective events are otherwise inhibited because of horizontally homogenous conditions of capped ascent. [Stevens et al. \(2005\)](#) found that POCs are long-lived, self-sustaining convective circulations that act to increase local rain frequency and volume by their convective cell structure. This structure is likely determined by combinations of entrainment of warm free-tropospheric air and local aerosol types and concentrations via their effects on cloud drop size distributions. The analysis conducted here suggests that these precipitation patterns exhibit a very irregular spatial pattern, with many CPEs positioned close to one another within POCs and longer distances of non-precipitation between POCs, particularly during the local winter (JJA) and spring [September–November (SON)] when shape factors and scale lengths are reduced to 0.40–0.55 and 75–100 km, respectively. The POCs serve as a contributing element to the decreased values of shape factor and scale length in the SEP through increased PoP(1) and variability in event spacing.

Large differences in the characteristic spatial patterns of precipitation systems are also evident between land and ocean areas. In addition to having generally lower PoP(1) reported by the 2CPC, the land areas in [Fig. 4](#) are characterized by lower CPE density characteristic of extensive precipitation systems. These results are consistent with [Gebremichael et al. \(2008\)](#), who found that spatial distributions using the TRMM PR follow a comparable land–ocean pattern through a scaling parameter that similarly represents the spatial extent of precipitation. This is corroborated by [Yang and Nesbitt \(2014\)](#), who observed more convective precipitation over land areas than ocean areas with the TRMM PR. [Williams and Stanfill \(2002\)](#) used the TRMM lightning imaging sensor to find that land areas are characterized by increased lightning flashes, which is a good proxy for convective activity.

There are some notable exceptions to the land–ocean contrast, including large regions in northern South America and the Weddell Sea. The landlike character of precipitation over the Weddell Sea is likely due to the persistent sea ice coverage and strong influence of the Antarctic ice sheet in this region. In the Southern Hemisphere summer months of December–February

(DJF), precipitation assumes shorter scale lengths more characteristic of the surrounding southern oceans. The Arctic Ocean follows a similar trend with scale lengths more characteristic of oceanic regions during the northern summer months. It is also interesting to note that the land–ocean contrast in scale length is broken along the Pacific coast of Canada and Alaska, where high precipitation frequency from storm-track systems flows over the Canadian Rocky Mountains. The Tibetan Plateau also exhibits low-scale lengths associated with high PoP(1), especially in boreal summer JJA during the South Asian monsoon southwesterly phase.

Precipitation in the Amazon more closely resembles oceanic precipitation than overland precipitation, especially during the wet season [DJF and March–May (MAM)]. Thus, the analysis here lends support to previous studies that have described the region as the Amazon Green Ocean (AGO; [Silva Dias et al. 2002](#); [Petersen et al. 2002](#); [Williams et al. 2002](#)). This region is discussed in greater depth below in the context of changes in precipitation scaling associated with easterly and westerly wind regimes during the wet season.

One of the shortcomings of *CloudSat*'s sun-synchronous orbit within the A-Train is that it only samples at about 0130 and 1330 local time (LT) ([L'Ecuyer and Jiang 2010](#)). As a result, it fails to resolve the full diurnal cycle of precipitation and may miss the peak of afternoon convection over land in areas with significant diurnal variation. For example, [Carbone et al. \(2002\)](#) demonstrate diurnal and semidiurnal signals in NEXRAD echo frequency over the midwestern United States during the May–August warm season. The *CloudSat* samples these areas just before the typical 2100–0200 UTC (Rockies) and 1900–0200 UTC (94°–82°W) peaks in echo frequency (not shown). The peak in precipitation intensity does not, however, necessarily coincide with the peak in precipitation frequency or the characteristic CPE geographic distribution. Still, the ascending and descending branches of the *CloudSat* orbit may be used to obtain a crude representation of day/night differences in the characteristics of precipitation.

Day/night variability of PoP(1), shape factor, and scale length is shown in [Fig. 5](#) as the ratio of values obtained by separate analysis of observations from daytime to nighttime D/N . The display of D/N is symmetric about one (note the nonlinear color scales) and omits areas that experience PoP(1) < 1% in either day or night overpasses. The analysis is identical to that of [Fig. 4](#) except the ~1330 LT daytime overpasses have been separated from and divided by the ~0130 LT nighttime overpasses.

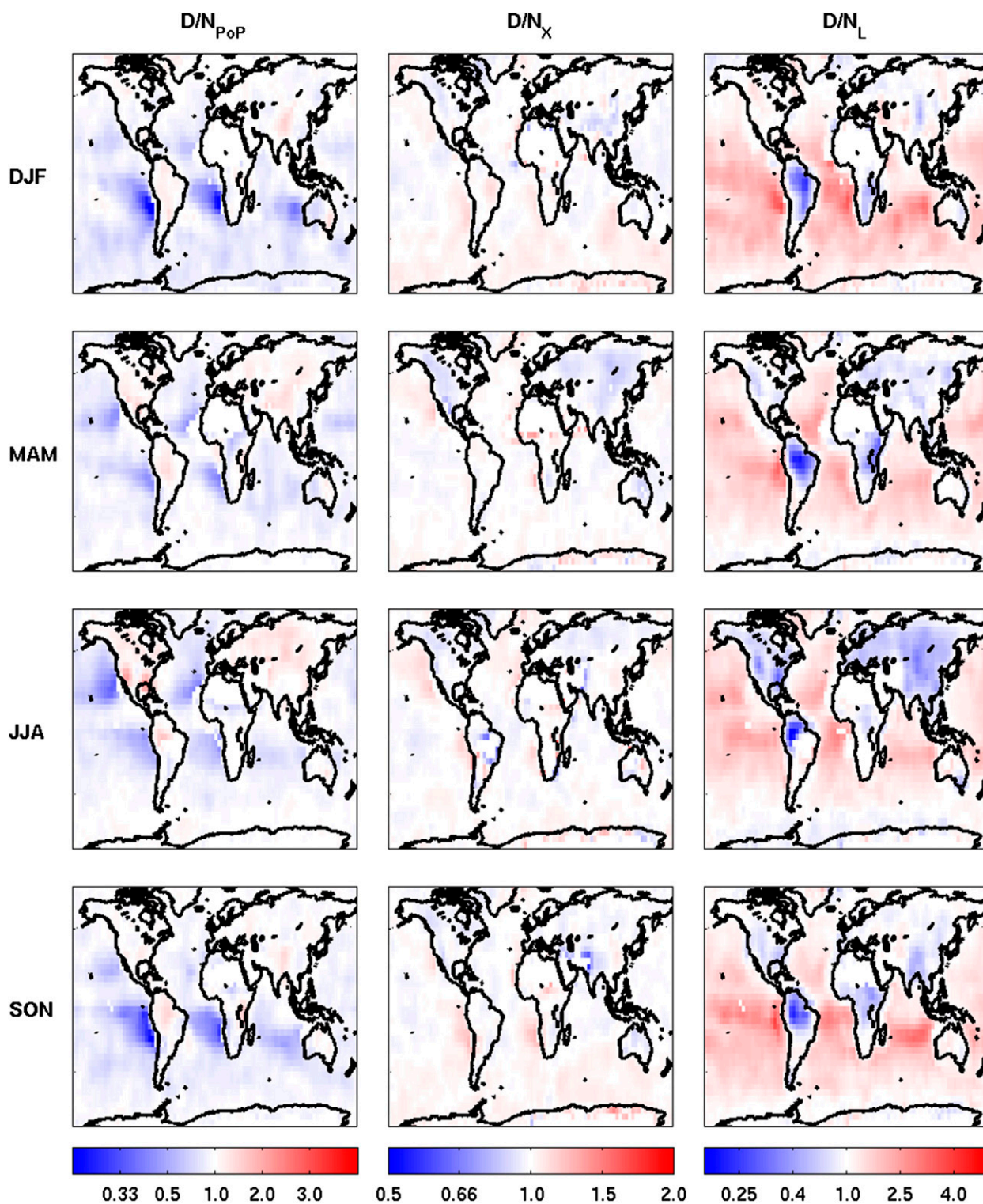


FIG. 5. Day/night $PoP(1)$, shape factor, and scale length expressed as the ratio of the day-to-night value at each $4^\circ \times 4^\circ$ location. All data for which $PoP(1) > 1\%$ are displayed, and the data have been filtered by Eq. (2).

It is clear from Fig. 5 that *CloudSat* observes the greatest day/night variation in the stratocumulus regions to the west of the subtropical continents. The D/N_{PoP} is far below 1 to the west of subtropical South America and Africa, with far more precipitation observed during the nighttime overpasses. This is consistent with Rapp et al. (2013), who report that 60%–80% of precipitation occurrence observed by *CloudSat* in the SEP is observed during the nighttime overpasses. On the other hand, continental areas tend to experience more precipitation during the daytime via convective processes, including the Amazon despite its otherwise oceanic spatial distribution characteristics. The results in Fig. 5 are generally consistent with previous studies that identified an oceanic diurnal maximum in the early morning hours (0300–0600) and a continental diurnal maximum in the afternoon hours (1500–1800) in TRMM to diagnose the peaks in the tropical and subtropical diurnal cycles of precipitation volume (Yang and Smith 2006; Yang et al. 2008; Yang and Smith 2008). In addition to the afternoon maxima in NEXRAD echo frequency over the Rocky Mountains and areas east of 94°W, Carbone et al. (2002) identified a consistent radar echo propagating eastward from the Rocky Mountains diurnal maximum in the afternoon. This propagating system arrives at the 98°–94°W area out of phase with the dominant diurnal cycle in the Rockies and the eastern areas. This out-of-phase system appears in JJA, where D/N_{PoP} drops below unity in the center of the United States, as indicated by higher precipitation frequency at night than during daytime overpasses.

The shape factor also exhibits its greatest day/night variations in the stratocumulus areas, with daytime overpasses having more evenly spaced precipitation events (higher shape factors) than nighttime overpasses. Small D/N_X over eastern Asia during MAM (and generally over land areas) indicates the opposite, with the precipitation event spacing being more uniform during the nighttime overpasses (larger shape factors at night). This is also observed in MAM shape factors over western North America.

The land–ocean contrast similarly dominates the day/night differences in scale length. In addition, oceanic stratocumulus regions exhibit daytime scale lengths up to 4 times as long as those at night. This indicates that these oceanic precipitation systems occur more frequently at night (see D/N_{PoP} column). On the other hand, D/N_L over land trends show longer scale lengths during the night, especially over northern South America where daytime convection dominates the diurnal rain cycle. Over northern midlatitude continents D/N_L is smallest during boreal summer JJA, reflecting the more solar convection-driven

TABLE 3. Mean magnitudes of day-to-night ratio from Fig. 5 as a function of season and hemisphere. Hemispheric summer is listed above winter in each case. Day/night variability is greatest in local summer in each hemisphere and variable.

	D/N_{PoP}	D/N_X	D/N_L
Northern Hemisphere	0.21 JJA	0.04 JJA	0.48 JJA
	0.11 DJF	0.03 DJF	0.24 DJF
Southern Hemisphere	0.30 DJF	0.04 DJF	0.63 DJF
	0.15 JJA	0.03 JJA	0.37 JJA

precipitation during those months than the frontal precipitation systems that characterize the northern winters of DJF. This is also, to a lesser degree, apparent in the northern midlatitude oceans but with opposite sign.

More generally, qualitative inspection of Fig. 5 reveals a tendency for the magnitude of the day/night variability to follow the seasonal cycle, with greater variability during the local summer. This is less evident in the D/N_X , where there is less day/night variability in the relative spacing of precipitation systems than in PoP (1) and scale length. The mean magnitudes of D/N are displayed in Table 3 for each hemisphere for JJA and DJF. In all cases, day/night variability is greatest in the hemispheric summer. This is likely caused by the increased convective precipitation during the summer than during the winter (Yang and Smith 2008). Stratiform precipitation responds less to diurnal solar forcing than convective precipitation.

Seasonal variations in the spatial character of precipitation are also evident in the distribution parameters in most areas. Figure 6 presents monthly shape factors and scale lengths for three regions that exhibit distinct seasonality in the distribution of precipitation. The behavior of the distribution parameters in the tropical west Pacific is also presented as a reference since this region does not exhibit strong seasonal variations throughout the region as a whole. Zonal fluctuations in precipitation volume maxima (Chen et al. 2003; Grose et al. 2014) associated with the seasonal migration of convection within the tropical west Pacific are generally contained within the boundaries defined in this study and are therefore not obvious in Fig. 6. Figure 6a shows variations in shape factor represent seasonal changes in the relative spacing of precipitation events. For example, the SEP experiences a range from 0.81 in the austral summer to about 0.62 in the austral winter. This range denotes a regime change from more evenly spaced precipitation events to a more clustered spatial distribution. The SEP cycle is out of phase with the Amazon, which experiences its maximum uniformity during the premonsoon months of August, September, and October (Williams

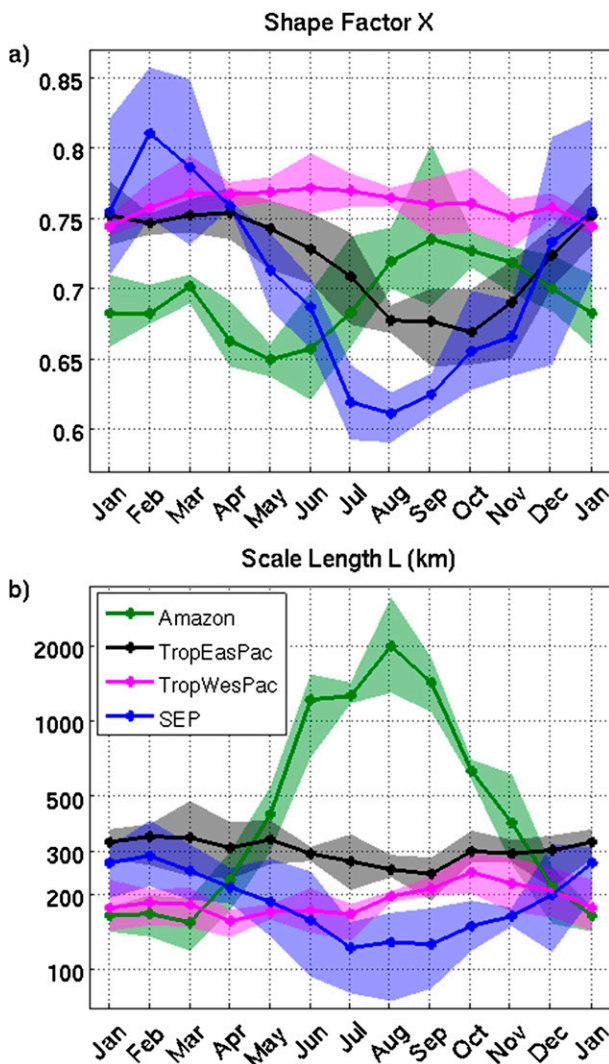


FIG. 6. The annual cycles of distribution parameters for 2007–10 for the Amazon (15°S – 0° , 290° – 310°E), tropical east Pacific (10°S – 10°N , 220° – 280°E), tropical west Pacific (10°S – 10°N , 130° – 190°E), and SEP (25° – 10°S , 250° – 284°E) regions. Solid lines show the mean monthly distribution parameter of the four years, and the shaded area bounds the maxima and minima from 2007 to 2010.

et al. 2002). In Fig. 6b, the Amazon exhibits the greatest change in scale length throughout the year, with the wet season (December–March) characterized by much smaller systems (Petersen et al. 2002; Williams et al. 2002) and the dry season featuring further widespread systems with scale lengths increasing to about 2000 km associated with monsoonal circulations. Scale length seasonal variability in other regions tends to be smaller than in the Amazon, although the SEP undergoes changes by a factor of 2, ranging from about 130 to 300 km between the periods of July–September and January–March, respectively. Precipitation in the tropical east Pacific also exhibits a seasonal

cycle in scale length but at a smaller relative range from ~ 250 to ~ 350 km.

6. Variability in the SEP stratocumulus to trade cumulus transition zone

The spatial characteristics of precipitation in the SEP exhibit a particularly strong seasonality that is worthy of closer inspection. Of particular significance is the geographic transition from predominantly stratocumulus to trade cumulus cloud regimes westward from the South American coast into the Pacific Ocean west of the SEP. The mean boundary layer winds are southerly in this region, so the transition outlined here is geographic and therefore does not follow the evolution of individual precipitation systems. This SEP transition zone (SEPTZ) is marked by decreasing lower-tropospheric stability (LTS), as shown in Fig. 7a, and increasing boundary layer heights as ocean surface temperatures warm away from the ocean upwelling near South America. Figure 7b outlines the SEPTZ over an example GOES visible image showing characteristic open-cellular convection at the western edge and closed-cell stratocumulus clouds at the eastern edge.

Figure 8 shows the variation in shape factor and scale length parameters across the SEPTZ. Resolution-degraded precipitation flags are sorted into 2.50° longitudinal bins for the geographical range illustrated on the map in Fig. 7. In general, precipitation events are more evenly spaced (indicated by a larger shape factor) in the summer than in the winter across the SEPTZ. This is consistent with the results of Rapp et al. (2013), who used *CloudSat* precipitation estimates to show that more precipitation falls in the austral winter (JJA) months than in the austral summer months. In addition to the increase in precipitation during the JJA season, there is also a difference in the spatial distribution of the rain events, with winter precipitation becoming more clustered, causing increased variability in the distances between CPEs.

Of particular interest in Fig. 8 is the SEPTZ from trade cumulus to stratocumulus, observed here roughly between longitudes from about 250° to 270°E . The westward transition from irregularly spaced to more uniformly spaced precipitation events is apparent in both seasons but the corresponding reduction in scale length is much more distinct in austral winter (JJA). Sharp increases in scale length at the eastern limits of the region are likely a result of constructive effects from the shallow boundary layers and aerosols from the coast of South America. The *CloudSat* 2CPC algorithm exploits the attenuation-corrected reflectivities in the fourth range bin above the surface because of the possibility of

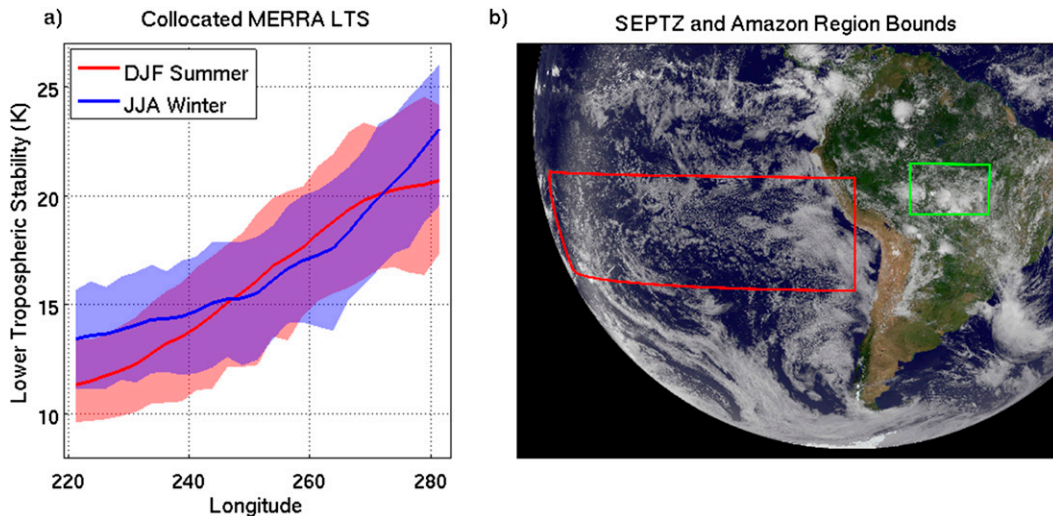


FIG. 7. (a) Mean and 10% and 90% quantile ranges of MERRA LTS across the SEPTZ in austral summer (DJF) and winter (JJA). LTS is aggregated in 2.5° longitudinal bins and filtered with a $[1\ 3\ 1]$ moving average for consistency with Figs. 8 and 9. (b) *GOES-13* image from 1445 UTC 13 Dec 2014 showing a transition from stratocumulus to trade cumulus convection to the west. Region bounds for the SEPTZ (red) and Amazon (green) are shown for reference.

surface clutter in the lowest range bins (Haynes et al. 2009). Burleyson et al. (2013) find drizzle to be less frequent nearer the coast along 20°S when using a shipborne W-band radar during the VAMOS Ocean–Cloud–Atmosphere–Land Study Regional Experiment

(VOCALS-REx) field campaign. They note that the decrease in drizzle rates near the coast is associated with higher aerosol concentrations and shallower boundary layers. In addition, Leon et al. (2008) showed that, because of surface clutter effects, the low cloud tops near

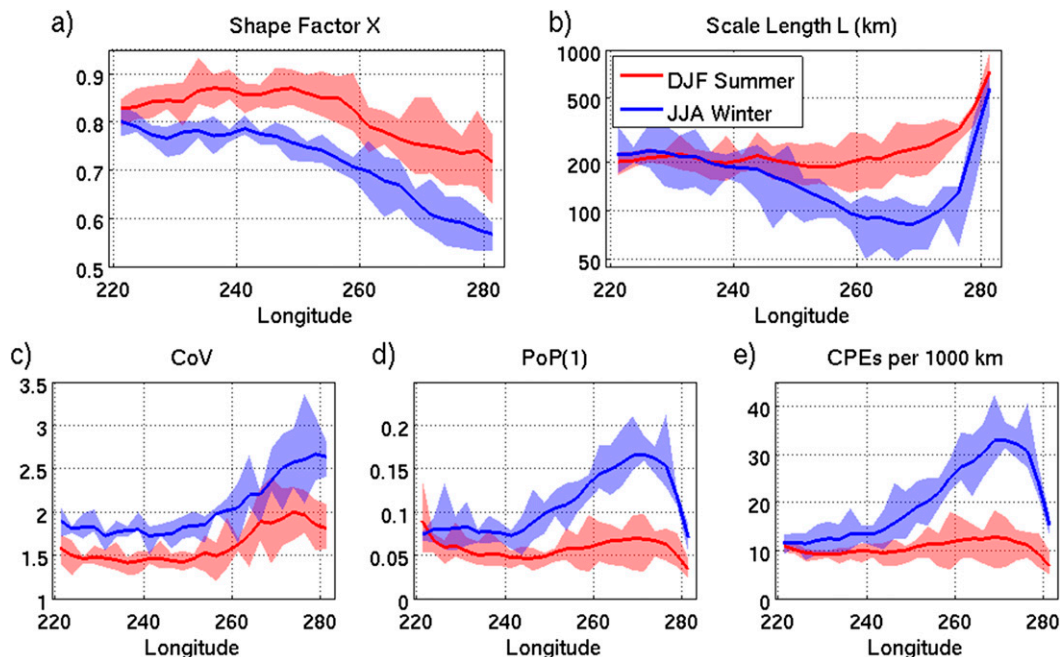


FIG. 8. Local summer and winter SEPTZ distribution parameters and their drivers. Precipitation data within the SEPTZ (25° – 10°S , 220° – 281.25°E) are partitioned into 2.5° zonal bins and the distribution parameters are computed via Eq. (1). Thin solid lines show the $[1\ 3\ 1]$ moving average of the 4-yr mean of *CloudSat* orbits passing over each area. Shaded regions bound the 4-yr extremes observed at each location.

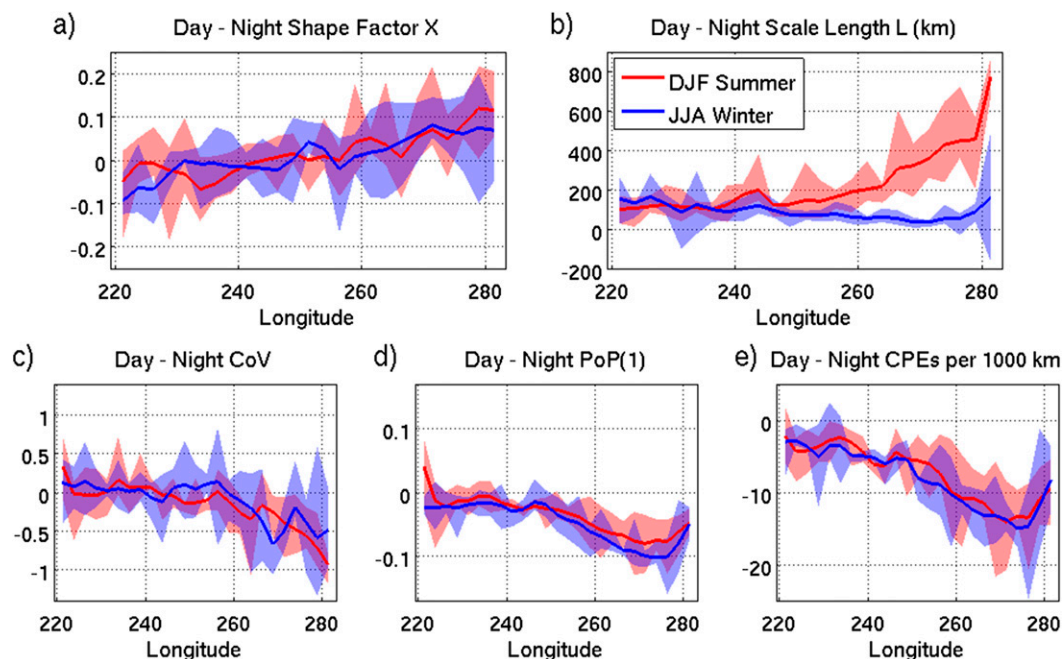


FIG. 9. As in Fig. 8, but showing day-minus-night differences between ascending (~ 1330 LT) and descending (~ 0130 LT) overpasses.

the coast affect *CloudSat* detections more often than areas with higher cloud tops. These effects suggest that the long scale lengths east of 280°E likely result from a combination of both decreased drizzle frequency and decreased detection rates due to low boundary layer heights and the precipitation inhibition aerosol effect.

Figures 4 and 8 show that the center of the signal from the SEP stratocumulus region shape factors occurs near $270^{\circ}\text{--}275^{\circ}\text{E}$. Moving west from this area, shape factors steadily rise before reaching a value characteristic of trade cumulus at 240°E . Wood and Hartmann (2006) report a similar general east-to-west progression of closed- to open-cell convection across the SEPTZ. In their case as well as here, the gradual transitions are representative of the averages of many sharp transitions in cloud and precipitation distributions as illustrated by Fig. 7b.

The westward progression from stratocumulus POC-type precipitation at around 270°E to more isolated cumulus precipitation is well documented (Wood and Hartmann 2006), and the analysis presented here demonstrates that the scaling approach outlined above captures the structural differences associated with differences in atmospheric stability across the SEPTZ with a relatively simple two-parameter exponential distribution. This is further demonstrated by Figs. 8c–e in collocated measures of CoV, PoP(1), and CPE density. In the eastern stratocumulus regime, the CoV is relatively high but decreases westward with the transition

to open cumulus causing the shape factor to increase. In the winter months, the scale length increases westward across the SEPTZ as the precipitation frequency and CPE density decrease. Austral summertime scale lengths do not exhibit a defined trend across the region, indicative of the fact that the PoP(1) and CPE density do not vary appreciably. The combination of changes in shape factor and scale length therefore indicates that while the prevalence of precipitation does not change across the SEPTZ in the summer months, the relative spatial distribution of the existing CPEs varies from east to west where eastern systems have a higher relative variance in their locations and the western systems are more evenly spread geographically.

7. Diurnal variability in the stratocumulus to cumulus transition zone

Rapp et al. (2013) found that *CloudSat* observes more precipitation in the SEP during its nighttime overpasses (~ 0130 LT) than during the daytime (~ 1330 LT). These differences extend to the spatial distribution of the precipitation as well. Figure 9 presents the differences in scaling distribution parameters when they are segregated into ascending or descending orbits that correspond to daytime and nighttime conditions, respectively. The day-minus-night differences in shape factor increase from west to east, with the largest differences (absolute and relative) associated with stratocumulus in

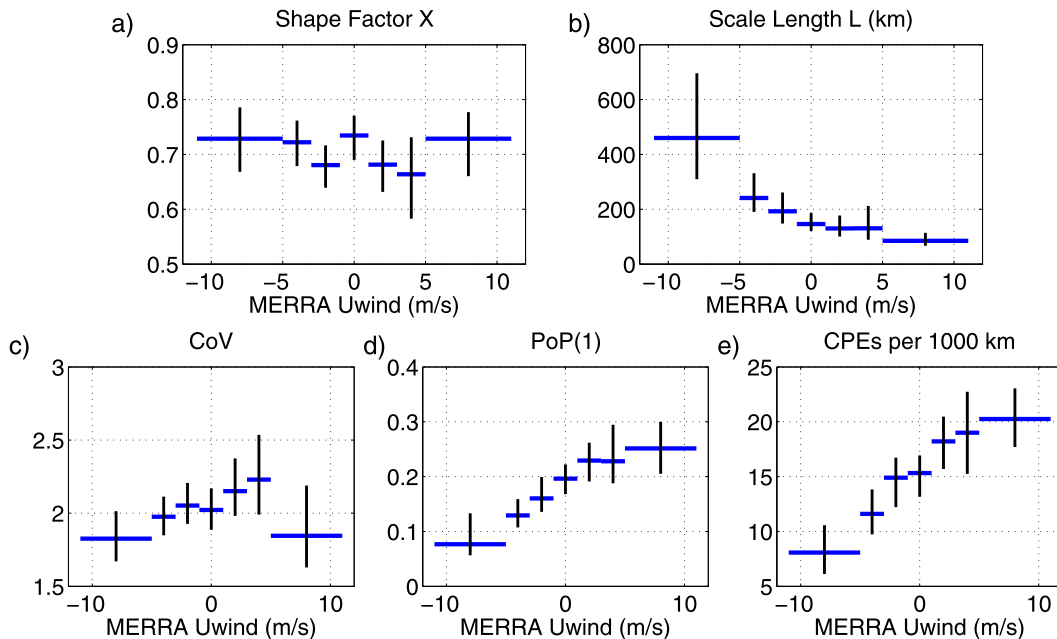


FIG. 10. Amazon wet-season distribution parameters and their associated spatial properties. Precipitation data composited by MERRA 800-hPa zonal wind strength are fitted with Eq. (1), and the 95% confidence intervals are computed via BCa bootstrap resampling, as explained in the text.

the far eastern side of the region. This corresponds to the fact that, in both seasons considered, there is greater variability in CPE spacing at night in the eastern stratocumulus region whereas there is greater variability in CPE spacing during the day in the trade cumulus region in the west. The scale length also exhibits day–night variations from west to east across the SEPTZ, especially in the summer months where scale lengths can differ by more than 700 km within the eastern areas near the South American coast. *CloudSat* observes very little near-coast precipitation during its daytime overpasses. Geographic changes in summer scale length follow the changes in the day–night PoP(1) and CPE density, but the winter day–night scale length differences do not. This is due to the smaller relative day–night changes in PoP(1) and CPE density during the winter than in the summer. Day–night differences in PoP(1) and CPE density are similar between the seasons, but the relative day–night changes in PoP(1) and CPE density are much greater in the summer months than the winter months, so day–night differences in scale lengths are strongest during the summer.

8. Amazon wet-season connection to zonal wind speed

Figure 4 demonstrates that the Amazon is somewhat distinct from other land surfaces in that it exhibits scale lengths that more closely resemble oceanic precipitation

than continental precipitation. Other studies document similar findings over the Amazon during the local wet season in the westerly wind regime. Williams et al. (2002) and Petersen et al. (2002), for example, find that precipitation during the wet-season westerly regime is more widespread, there are fewer lightning flashes, cloud tops are lower, and there are fewer cloud condensation nuclei compared to surrounding land areas and to other times of the year. This has led to the moniker AGO for the wet-season westerly wind regime. Williams et al. (2002) also find that the westerly regime is associated with more widespread precipitation events rather than the isolated convection that is more common during the dry season. It is reasonable to ask whether similar subseasonal relationships to local zonal wind direction can be deduced from the precipitation distribution parameters.

Figure 10 shows the distribution parameters and their associated spatial properties composited with Modern-Era Retrospective Analysis for Research and Applications (MERRA) zonal wind strength within the geographic region bounded by 15°–9°S, 295°–310°E (consistent with Petersen et al. 2002). The shape factor and CoV show little dependence on the large-scale zonal wind speed and direction, but the scale length correlates strongly as do the native-resolution PoP(1) and CPE density. The Amazon westerly regime is marked in Fig. 10 by shorter scale lengths and high PoP(1) and CPE densities associated with widespread precipitation, which is in agreement with Petersen et al. (2002).

Because the latitude range of the data selected for Fig. 10 is limited to 6° , additional care was taken to ensure each plotted value contained enough data to hold uncertainties to an acceptable level. The shape factor in Eq. (1) makes the regressions very flexible to variations in the precipitation data so confidence intervals based on errors in the fit, alone, tend to be too small to encompass the sampling uncertainty inherent in using discrete *CloudSat* overpasses. To better represent sampling uncertainties, the 95% confidence intervals shown in Fig. 10 were computed using the bias-corrected and accelerated (BCa) bootstrap method. An outline for BCa bootstrap confidence intervals can be found in Wilks (2011) and is summarized here.

The bootstrap resampling technique (Efron 1979) consists of drawing N random samples with replacement from the original N overpasses. The number of overpasses belonging to each Amazon zonal wind bin ranges from 49 to 128, with more overpasses near zero zonal wind speed. Because the latitude span is so short, resolution-degraded precipitation flags from each overpass are converted to PoP(d) and treated as a single measurement with a single degree of freedom in the collection of overpasses. Collocated MERRA zonal winds are also averaged, and the overpasses with zonal wind standard deviation greater than 99% of other overpasses (standard deviation of about 4.1 m s^{-1}) are discarded to ensure that the mean winds represent the precipitation regime throughout the overpass.

After the resampled distribution is created for an individual zonal wind bin, the BCa confidence intervals (Efron 1987; Efron and Tibshirani 1993) are formed. The BCa process makes no assumptions about the symmetry or bias of the sample distribution and so the resulting confidence intervals are not necessarily symmetric and do not necessarily correspond to CDF values of 0.025 and 0.975 for an $\alpha = 0.95$ two-tailed confidence level. This is most relevant for the scale length, whose distribution is generally asymmetric with a tail toward longer lengths, especially over land. The acceleration parameter corrects for asymmetric or skewed sampling distributions and is computed from jackknife estimates of the parameter of interest (e.g., shape factor, CPE density). The BCa confidence intervals are much more representative of sampling uncertainty than the R -square fit errors, alone, but the significance of the relation between Amazon wet-season scale length and zonal wind speed is preserved.

9. Discussion

This study introduces a new method of describing variations in precipitation occurrence as a function of

spatial resolution using an exponential structure function with two free parameters. The shape factor X describes the relative spatial locations of distinct precipitation events, while the scale length L describes the spatial density of the CPEs and their size [via PoP(1)]. These attributes of precipitation constitute key factors governing local hydrologic cycles, surface runoff models, latent and radiative heat distributions, and statistical downscaling.

Global and seasonal variations in the shape factor and scale length generally follow well-understood patterns of frequently used measures of large-scale thermodynamics and also correlate with local meteorological weather regimes. For example, the distribution parameters both exhibit variations consistent with the east–west transition from stratocumulus to trade cumulus cloud types in the SEPTZ. The shape factor and scale length capture clear distinctions between the highly variable stratocumulus-topped precipitation in the east and the open-cell convection in the west. These differences can be directly related to differences in characteristics of the spatial distribution of precipitation: CPE relative spacing, PoP(1), and the CPE density. Furthermore, the scale lengths over the Amazon during the wet season are found to correlate with local zonal wind speed, with westerlies favoring high PoP(1) and large areal extent, consistent with previous reports of wet-season regime differences.

The high sensitivity of the W-band CPR aboard *CloudSat* to detecting precipitation is central to this study. Unfortunately, the one-dimensional nature of CPR observations limits its instantaneous measurements to the nearly meridional direction at low and midlatitudes. This could introduce a bias in areas where precipitation exhibits a preferred orientation and is expected to be most relevant over large landmasses that experience preferential directionality, as is the case with frontal systems. The application of this procedure to stochastic downscaling would benefit greatly from knowledge of the 2D structure of occurrence, which is something a one-dimensional precipitation flag cannot offer. The newly launched Global Precipitation Measurement (GPM) spacecraft carries the dual-frequency precipitation radar (DPR) at Ku and Ka bands. The global coverage and increased sensitivity over the TRMM PR (Ka band versus Ku band) could assist this technique, but with a sensitivity of 12 dBZ and a 4-km FoV, some broken and light precipitation will likely still escape detection, especially in areas characterized by light or frozen precipitation, leading to uncertainty in the steep slopes at fine resolutions in Fig. 1 and Fig. 2.

The analysis presented here has potentially wide-ranging applications into understanding the spatial

distribution of precipitation. Hydrologic forecasters require high-resolution information of the structure of precipitation to predict the impact of flood events. Such high temporal and spatial resolution is not yet available from large-scale forecast models, so precipitation data must be downscaled either dynamically or statistically to the catchment scale, often only a few square kilometers. The method introduced here is computationally efficient and is therefore possible to implement without the additional expense of an MMF, nested CRM, or a large-eddy simulation. The global modeling community may also use this methodology to parameterize subgrid variations in precipitation within a grid box, where spatial distributions of precipitation events are created stochastically and are influenced by estimated shape factors and scale lengths. Though the insights provided by examining the variation of these parameters in the south-central Amazon and SEPTZ are not entirely new in light of previous studies, they confirm that distribution parameters are often correlated with local state variables that are already estimated at the grid box and time step scale (e.g., CAPE, wind speed, surface temperature). Analyses of more general drivers of X and L for such global modeling applications is ongoing.

Acknowledgments. The authors thank the GOES team (goes.gsfc.nasa.gov) for their publication of freely available processed true color imagery. This research was supported by NASA CloudSat/CALIPSO Science Team (CCST) Grant NNX13AQ32G.

REFERENCES

- Berg, W., T. S. L'Ecuyer, and J. M. Haynes, 2010: The distribution of rainfall over oceans from spaceborne radars. *J. Appl. Meteor. Climatol.*, **49**, 535–543, doi:[10.1175/2009JAMC2330.1](https://doi.org/10.1175/2009JAMC2330.1).
- Burleyson, C., S. P. de Szoeke, S. E. Yuter, M. Wilbanks, and W. A. Brewer, 2013: Ship-based observations of the diurnal cycle of southeast Pacific marine stratocumulus clouds and precipitation. *J. Atmos. Sci.*, **70**, 3876–3894, doi:[10.1175/JAS-D-13-01.1](https://doi.org/10.1175/JAS-D-13-01.1).
- Carbone, R. E., J. D. Tuttle, D. A. Ahijevych, and S. B. Trier, 2002: Inferences of predictability associated with warm season precipitation episodes. *J. Atmos. Sci.*, **59**, 2033–2056, doi:[10.1175/1520-0469\(2002\)059<2033:IOPAWW>2.0.CO;2](https://doi.org/10.1175/1520-0469(2002)059<2033:IOPAWW>2.0.CO;2).
- Chen, G., J. Ma, C. Fang, and Y. Han, 2003: Global oceanic precipitation derived from TOPEX and TMR: Climatology and variability. *J. Climate*, **16**, 3888–3904, doi:[10.1175/1520-0442\(2003\)016<3888:GOPDFT>2.0.CO;2](https://doi.org/10.1175/1520-0442(2003)016<3888:GOPDFT>2.0.CO;2).
- Efron, B., 1979: Bootstrap methods: Another look at the jackknife. *Ann. Stat.*, **7**, 1–26, doi:[10.1214/aos/1176344552](https://doi.org/10.1214/aos/1176344552).
- , 1987: Better bootstrap confidence intervals. *J. Amer. Stat. Assoc.*, **82**, 171–185, doi:[10.1080/01621459.1987.10478410](https://doi.org/10.1080/01621459.1987.10478410).
- , and R. J. Tibshirani, 1993: *An Introduction to the Bootstrap*. Chapman and Hall, 436 pp.
- Ferraris, L., S. Gabellani, N. Rebora, and A. Provenzale, 2003: A comparison of stochastic models for spatial rainfall downscaling. *Water Resour. Res.*, **39**, 1368, doi:[10.1029/2003WR002504](https://doi.org/10.1029/2003WR002504).
- Flato, G., and Coauthors, 2013: Evaluation of climate models. *Climate Change 2013: The Physical Science Basis*, T. F. Stocker et al., Eds., Cambridge University Press, 741–866.
- Fowler, H., S. Blenkinsop, and C. Tebaldi, 2007: Linking climate change modelling to impacts studies: Recent advances in downscaling techniques for hydrological modelling. *Int. J. Climatol.*, **27**, 1547–1578, doi:[10.1002/joc.1556](https://doi.org/10.1002/joc.1556).
- Gebremichael, M., W. F. Krajewski, T. M. Over, Y. N. Takayabu, P. Arkin, and M. Katayama, 2008: Scaling of tropical rainfall as observed by TRMM precipitation radar. *Atmos. Res.*, **88**, 337–354, doi:[10.1016/j.atmosres.2007.11.028](https://doi.org/10.1016/j.atmosres.2007.11.028).
- Grose, M. R., and Coauthors, 2014: Assessment of the CMIP5 global climate model simulations of the western tropical Pacific climate system and comparison to CMIP3. *Int. J. Climatol.*, **34**, 3382–3399, doi:[10.1002/joc.3916](https://doi.org/10.1002/joc.3916).
- Haynes, J. M., T. S. L'Ecuyer, G. L. Stephens, S. D. Miller, C. Mitrescu, N. B. Wood, and S. Tanelli, 2009: Rainfall retrieval over the ocean with spaceborne W-band radar. *J. Geophys. Res.*, **114**, D00A22, doi:[10.1029/2008JD009973](https://doi.org/10.1029/2008JD009973).
- Hoskins, B. J., and K. I. Hodges, 2005: A new perspective on Southern Hemisphere storm tracks. *J. Climate*, **18**, 4108–4129, doi:[10.1175/JCLI3570.1](https://doi.org/10.1175/JCLI3570.1).
- Kundu, P. K., and R. K. Siddani, 2011: Scale dependence of spatiotemporal intermittence of rain. *Water Resour. Res.*, **47**, W08522, doi:[10.1029/2010WR010070](https://doi.org/10.1029/2010WR010070).
- L'Ecuyer, T. S., and J. H. Jiang, 2010: Touring the atmosphere aboard the A-Train. *Phys. Today*, **63**, 36–41, doi:[10.1063/1.3463626](https://doi.org/10.1063/1.3463626).
- Leon, D. C., Z. Wang, and D. Liu, 2008: Climatology of drizzle in marine boundary layer clouds based on 1 year of data from CloudSat and Cloud-Aerosol Lidar and Infrared Pathfinder Satellite Observations (CALIPSO). *J. Geophys. Res.*, **113**, D00A14, doi:[10.1029/2008JD009835](https://doi.org/10.1029/2008JD009835).
- Marani, M., 2005: Non-power-law-scale properties of rainfall in space and time. *Water Resour. Res.*, **41**, W08413, doi:[10.1029/2004WR003822](https://doi.org/10.1029/2004WR003822).
- Marchand, R., 2012: Spatial correlation of hydrometeor occurrence, reflectivity, and rain rate from CloudSat. *J. Geophys. Res.*, **117**, D06202, doi:[10.1029/2011JD016678](https://doi.org/10.1029/2011JD016678).
- Milly, P. C. D., J. Betancourt, M. Falkenmark, R. M. Hirsch, Z. W. Kundzewicz, D. P. Lettenmaier, and R. J. Stouffer, 2008: Stationarity is dead: Whither water management? *Science*, **319**, 573–574, doi:[10.1126/science.1151915](https://doi.org/10.1126/science.1151915).
- O'Brien, T. A., F. Li, W. D. Collins, S. A. Rauscher, T. D. Ringler, M. Taylor, S. M. Hagos, and L. R. Leung, 2013: Observed scaling in clouds and precipitation and scale incognizance in regional to global atmospheric models. *J. Climate*, **26**, 9313–9333, doi:[10.1175/JCLI-D-13-00005.1](https://doi.org/10.1175/JCLI-D-13-00005.1).
- Petersen, W. A., S. W. Nesbitt, R. J. Blakeslee, R. Cifelli, P. Hein, and S. A. Rutledge, 2002: TRMM observations of intraseasonal variability in convective regimes over the Amazon. *J. Climate*, **15**, 1278–1294, doi:[10.1175/1520-0442\(2002\)015<1278:TOOIVI>2.0.CO;2](https://doi.org/10.1175/1520-0442(2002)015<1278:TOOIVI>2.0.CO;2).
- Rapp, A. D., M. Lebsock, and T. S. L'Ecuyer, 2013: Low cloud precipitation climatology in the southeastern Pacific marine stratocumulus region using CloudSat. *Environ. Res. Lett.*, **8**, 014027, doi:[10.1088/1748-9326/8/1/014027](https://doi.org/10.1088/1748-9326/8/1/014027).
- Schleiss, M., J. Jaffrain, and A. Berne, 2011: Statistical analysis of rainfall intermittency at small spatial and temporal scales. *Geophys. Res. Lett.*, **38**, L18403, doi:[10.1029/2011GL049000](https://doi.org/10.1029/2011GL049000).

- Silva Dias, M. A. F., and Coauthors, 2002: Cloud and rain processes in a biosphere-atmosphere interaction context in the Amazon region. *J. Geophys. Res.*, **107**, 8072, doi:[10.1029/2001JD000335](https://doi.org/10.1029/2001JD000335).
- Smalley, M., T. S. L'Ecuyer, M. Lebsock, and J. Haynes, 2014: A comparison of precipitation occurrence from the NCEP Stage IV QPE product and the *CloudSat* Cloud Profiling Radar. *J. Hydrometeor.*, **15**, 444–458, doi:[10.1175/JHM-D-13-048.1](https://doi.org/10.1175/JHM-D-13-048.1).
- Stephens, G. L., and Coauthors, 2010: Dreary state of precipitation in global models. *J. Geophys. Res.*, **115**, D24211, doi:[10.1029/2010JD014532](https://doi.org/10.1029/2010JD014532).
- Stevens, B., G. Vali, K. Comstock, R. Wood, M. C. Van Zanten, P. H. Austin, C. S. Bretherton, and D. H. Lenschow, 2005: Pockets of open cells and drizzle in marine stratocumulus. *Bull. Amer. Meteor. Soc.*, **86**, 51–57, doi:[10.1175/BAMS-86-1-51](https://doi.org/10.1175/BAMS-86-1-51).
- Tanelli, S., S. L. Durden, K. S. Pak, D. G. Reinke, P. Partain, J. M. Haynes, and R. T. Marchand, 2008: *CloudSat's* Cloud Profiling Radar after two years in orbit: Performance, calibration, and processing. *IEEE Trans. Geosci. Remote Sens.*, **46**, 3560–3573, doi:[10.1109/TGRS.2008.2002030](https://doi.org/10.1109/TGRS.2008.2002030).
- Tao, K., and A. P. Barros, 2010: Using fractal downscaling of satellite precipitation products for hydrometeorological applications. *J. Atmos. Oceanic Technol.*, **27**, 409–427, doi:[10.1175/2009JTECHA1219.1](https://doi.org/10.1175/2009JTECHA1219.1).
- Wilks, D. S., 2010: Use of stochastic weather generators for precipitation downscaling. *Wiley Interdiscip. Rev.: Climate Change*, **1**, 898–907, doi:[10.1002/wcc.85](https://doi.org/10.1002/wcc.85).
- , 2011: *Statistical Methods in the Atmospheric Sciences*. 3rd ed. Elsevier, 676 pp.
- Williams, E., and S. Stanfill, 2002: The physical origin of the land–ocean contrast in lightning activity. *C. R. Phys.*, **3**, 1277–1292, doi:[10.1016/S1631-0705\(02\)01407-X](https://doi.org/10.1016/S1631-0705(02)01407-X).
- , and Coauthors, 2002: Contrasting convective regimes over the Amazon: Implications for cloud electrification. *J. Geophys. Res.*, **107**, 8082, doi:[10.1029/2001JD000380](https://doi.org/10.1029/2001JD000380).
- Wood, R., 2012: Stratocumulus clouds. *Mon. Wea. Rev.*, **140**, 2373–2423, doi:[10.1175/MWR-D-11-00121.1](https://doi.org/10.1175/MWR-D-11-00121.1).
- , and D. L. Hartmann, 2006: Spatial variability of liquid water path in marine low cloud: The importance of mesoscale cellular convection. *J. Climate*, **19**, 1748–1764, doi:[10.1175/JCLI3702.1](https://doi.org/10.1175/JCLI3702.1).
- Yang, S., and E. A. Smith, 2006: Mechanisms for diurnal variability of global tropical rainfall observed from TRMM. *J. Climate*, **19**, 5190–5226, doi:[10.1175/JCLI3883.1](https://doi.org/10.1175/JCLI3883.1).
- , and —, 2008: Convective–stratiform precipitation variability at seasonal scale from eight years of TRMM observations. *J. Climate*, **21**, 4087–4114, doi:[10.1175/2008JCLI2096.1](https://doi.org/10.1175/2008JCLI2096.1).
- , and S. W. Nesbitt, 2014: Statistical properties of precipitation as observed by the TRMM precipitation radar. *Geophys. Res. Lett.*, **41**, 5636–5643, doi:[10.1002/2014GL060683](https://doi.org/10.1002/2014GL060683).
- , K. S. Kuo, and E. A. Smith, 2008: Persistent nature of secondary diurnal modes in both land and ocean precipitation. *J. Climate*, **21**, 4115–4131, doi:[10.1175/2008JCLI2140.1](https://doi.org/10.1175/2008JCLI2140.1).